

Discriminating the Phase of a Coherent Tone with a Flux-Switchable Superconducting Circuit

L. Di Palma^{1,2,*}, A. Miano³, P. Mastrovito¹, D. Massarotti^{4,5}, M. Arzeo², G.P. Pepe¹,
F. Tafuri^{1,6} and O. Mukhanov⁷

¹*Dipartimento di Fisica “Ettore Pancini”, Università degli Studi di Napoli Federico II, Napoli 80125, Italy*

²*SEEQC, Corso Protopisani, 70, Napoli 80146, Italy*


³*Department of Applied Physics, Yale University, New Haven, Connecticut 06520, USA*

⁴*Dipartimento di Ingegneria Elettrica e delle Tecnologie dell’Informazione, Università degli Studi di Napoli Federico II, via Claudio, Napoli 80125, Italy*

⁵*CNR-SPIN, UOS Napoli, Monte S. Angelo, via Cinthia, Napoli 80126, Italy*

⁶*CNR-Istituto Nazionale di Ottica (CNR-INO), Largo Enrico Fermi 6, Florence 50125, Italy*

⁷*SEEQC, Elmsford, New York 10523, USA*

 (Received 10 October 2022; revised 20 April 2023; accepted 1 May 2023; published 7 June 2023)

We propose a new phase detection technique based on a flux-switchable superconducting circuit, the Josephson digital phase detector (JDPD), which is capable of discriminating between two phase values of a coherent input tone. When properly excited by an external flux, the JDPD is able to switch from a single-minimum to a double-minima potential and, consequently, relax in one of the two stable configurations depending on the phase sign of the input tone. The result of this operation is digitally encoded in the occupation probability of a phase particle in either of the two JDPD wells. In this work, we demonstrate the working principle of the JDPD up to a frequency of 400 MHz with a remarkable agreement with theoretical expectations. As a future scenario, we discuss the implementation of this technique to superconducting qubit readout. We also examine the JDPD compatibility with the single-flux-quantum architecture, employed to fast-drive and measure the device state.

DOI: [10.1103/PhysRevApplied.19.064025](https://doi.org/10.1103/PhysRevApplied.19.064025)

I. INTRODUCTION

The detection of coherent tones is a crucial operation in many experiments, ranging from the detection of elusive particles [1–4] to quantum information processing [5–8]. In the last decades, the development of circuit quantum electrodynamics [9,10], based on superconducting devices, has led to a growing interest in measurements of microwave signals, which typically involve the use of superconducting cavities [5,11]. As an example of application, the readout of a superconducting qubit is commonly performed with a quantum nondemolition operation which relies on the frequency response of a co-located resonator, being dependent on the state of the qubit via dispersive coupling [10]. The cavity can be probed in reflection with a tone at a fixed frequency, encoding the state of the qubit in the relative phase and amplitude of the reflected pulse [6–8,12]. The first experiments that successfully performed the dispersive readout of a qubit with acceptable fidelities were designed to encode the information in the relative amplitude of the reflected pulse [10]. Later, the advent

of Josephson parametric amplifiers [13] made it possible to sense the phase response of the readout resonator with fidelities above 99%.

In the last several years, there has been growing interest in superconducting digital circuits [14–16], which operate with low power dissipation at cryogenic temperatures [17–19]. These devices have been proposed as control and readout interfaces for cryogenic circuits [20,21] with the goal to reduce hardware complexity and improve system scalability [22]. The state-of-the-art digital readout of microwave photons relies on the Josephson photomultiplier (JPM), which operates at the millikelvin stage of a dilution refrigerator [14,15,23]. The JPM consists of a bistable superconducting circuit whose operating point can be made sensitive to the average number of photons in the readout cavity. This information is mapped in the current direction flowing through the device [14,15]. A possible way to read the JPM’s state exploits propagating fluxons [24] produced by a single-flux-quantum (SFQ) classical circuit [16]. In this framework, JPM is proposed as part of a more complex architecture, in which classical qubit control, measurement, and data processing are performed by an SFQ processor. This approach can be a valid solution

*luigi.dipalma@unina.it

to enhance the scalability of superconducting quantum systems, which remains a big engineering challenge to realize practical error-corrected quantum computers [22].

Despite the advantages of such a detection technique, the JPM approach still requires an adiabatic externally generated flux bias in order to tune the device during the many steps necessary for successful quantum nondemolition [25] readout. Measurement is performed in resonance with the cavity and requires nontrivial operations to reduce the backaction on the quantum chip, which limits the readout speed. Moreover, the JPM protocol provides an intrinsically state-dependent fidelity that can be harmful in some experiments [14,15].

In this paper, we propose a new phase detection technique based on a flux-switchable superconducting circuit, which is capable of discriminating between two phase values of a coherent input tone. For instance, such a tone can be a readout pulse whose phase encodes the outcome of a qubit measurement. The device operation is compatible with SFQ circuits, which could be employed to perform the detection in a fully digital fashion. Our device is based on a bistable quantum flux parametron (QFP) [26,27], which has already been proposed for classical [4,28,29] and quantum applications, including superconducting flux qubits controlled with fast pulses [30–32] or ultralow-power logic devices [27]. In this technique, the QFP is at first flux-biased into a harmonic configuration to sense the input coherent tone, then quickly flux-switched to a bistable configuration to store the information on the tone’s phase. We name our device a “Josephson digital phase detector” (JDPD), since the result of the detection is naturally encoded in the occupation probability of a phase particle in either of two wells in the bistable configuration.

In this paper, we present a circuit model of the JDPD and discuss the operating principle, with some consideration on the symmetries required to achieve high performances and suppress the backaction due to the diabatic flux switch. Numerical simulations with QuTip [33] are performed, showing how the JDPD can perform phase detection with a fidelity of 99.99% when flux-switched on a time scale of 0.05 ns. From these results, we discuss the compatibility of the JDPD with SFQ technology. We also present experimental results on a preliminary device, which is capable of detecting the phase of a 400 MHz input coherent tone with a 99.98% fidelity when flux-switched on a time scale of 1 ns. The acquired data confirm the feasibility of the operating principle and are in very good agreement with numerical simulations adapted to our experimental scenario.

For future prospects, we discuss how we are currently implementing the next generation of experimental devices, which would be flux-switched by an integrated pulse generator based on SFQ logic to perform fast phase detection of a gigahertz input tone. SFQ circuits can also be employed to generate an input signal phase-locked to the

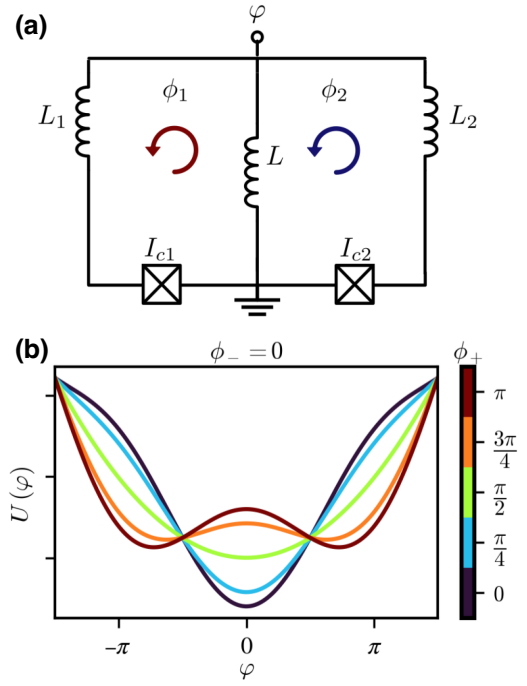


FIG. 1. Schematic of the Josephson digital phase detector (JDPD). (a) The JDPD is composed of a nominally symmetric quantum flux parametron (QFP), whose left and right loops are phase-biased by independent phases $\phi_{1(2)}$. The bias phases are related to the magnetic fluxes $\Phi_{1(2)}$ threaded to each loop by the relation $\phi_{1(2)} = 2\pi(\Phi_{1(2)}/\Phi_0)$. (b) Potential energy landscapes of the JDPD for different values of common flux $\phi_+ = (\phi_1 + \phi_2)/2$, for $\phi_- = (\phi_1 - \phi_2)/2 = 0$. The potential energy can present one absolute minimum (blue curve), harmonic potential landscape (green curve), or two absolute minima (red curve), depending on the external magnetic flux.

flux-switching pulse. We also address the compatibility with the JDPD approach applied to superconducting qubits readout and we envision its employment as digital readout modules in SFQ-based quantum information processing platforms, where the JDPD output is converted in SFQ form.

II. DEVICE MODEL

The fundamental block of a JDPD is based on a QFP [Fig. 1(a)], whose left and right loops can be independently flux-biased by, respectively, the normalized fluxes ϕ_1 and ϕ_2 :

$$\phi_{1,2} = 2\pi \frac{\Phi_{1,2}}{\Phi_0}. \quad (1)$$

Here $\Phi_{1,2}$ is the magnetic flux threaded, respectively, to the left and the right loops of the circuit in Fig. 1(a).

To describe the flux-tuning properties of the device in a compact form, it is useful to introduce the common and

differential fluxes ϕ_+ and ϕ_- , defined as

$$\begin{aligned}\phi_+ &= \frac{\phi_1 + \phi_2}{2}, \\ \phi_- &= \frac{\phi_1 - \phi_2}{2}.\end{aligned}\quad (2)$$

These can be independently generated by properly designed flux lines, as shown later in the experimental section of the paper (Sec. V). In the symmetrical case, where $I_{c1} = I_{c2} = I_c$, and neglecting the energy stored in the stray linear inductances under the assumption $L_{1,2} < L_J$, the potential energy function of the device is given by

$$\frac{U(\varphi)}{E_L} = \frac{\varphi^2}{2} - 2\beta_L \cos(\phi_+) \cos(\varphi + \phi_-), \quad (3)$$

where $\beta_L = 2\pi I_c L / \Phi_0$ and φ is the phase drop across the central inductor L . The potential energy in Eq. (3) is normalized to the linear inductor energy $E_L = (\Phi_0/2\pi)^2 / L$. This expression is formally identical to the potential energy of a double superconducting quantum interference device [30–32]. If $2\beta_L \leq 1$, the potential has only one absolute minimum for any combination of ϕ_{\pm} . If $2\beta_L > 1$, the bias fluxes can be tuned to generate potential shapes with multiple minima. For instance, in Fig. 1(b), for a device with $2\beta_L = 3$ and for $\phi_- = 0$, the potential energy can host a single absolute minimum for $\phi_+ = 0$ or two degenerate minima for $\phi_+ = \pi$. The device can also be flux-biased to a harmonic configuration for $\phi_+ = \pi/2$, where the nonlinear term in Eq. (3) is suppressed. The detection technique exploits the tunability of the JDPD's potential energy to perform phase detection.

The kinetic energy is given by capacitive contributions of the Josephson junctions inside the rf loops, i.e.,

$$T = 2 \frac{e^2}{2C} n^2 = 2E_c n^2, \quad (4)$$

where $C_1 = C_2 = C$ is assumed for both junction capacitances and n is the operator number. Assembling Eqs. (3) and (4), the static JDPD Hamiltonian reads as

$$H = 2E_c n^2 + E_L \left[\frac{\varphi^2}{2} - 2\beta \cos \phi_+ \cos(\varphi + \phi_-) \right]. \quad (5)$$

III. PRINCIPLE OF OPERATION

The diagram of the phase detection protocol is shown in Fig. 2. The protocol is composed of four separate steps, respectively labeled as “ready,” “detection,” “digitalization,” and “sense.” The JDPD is first configured in a harmonic shape, by providing $\phi_+ = \pi/2$, as shown in the first part of Fig. 2. The Hamiltonian in Eq. (5) takes the form

$$H_{\text{ho}} = 2E_c n^2 + E_L \varphi^2 = \hbar \omega_0 \left(\frac{1}{2} + a^\dagger a \right), \quad (6)$$

where $\omega_0 = \sqrt{4E_c E_L} / \hbar$ is the natural frequency of the equivalent harmonic oscillator. In the absence of any external perturbation, we expect the wave function to relax in the ground state of the potential, which makes the device “ready” to start phase detection.

In the “detection” step of Fig. 2, an input current stimulus $I(t)$ is applied through the JDPD input node. The system evolves according to the Hamiltonian of a driven harmonic oscillator,

$$H_{\text{tot}} = H_{\text{ho}} - \frac{\Phi_0 I(t)}{2\pi} \varphi. \quad (7)$$

For simplicity, we consider the case in which $I(t)$ is a sinusoidal tone with amplitude I_0 , angular frequency ω_r , and

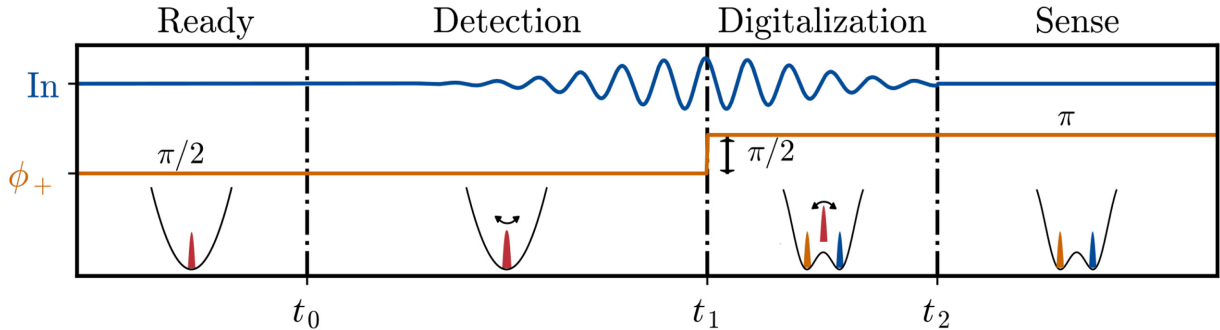


FIG. 2. Timing diagram of the phase detection performed with the JDPD. The detector is initially reset in the ground state of the harmonic configuration by applying $\phi_+ = \pi/2$. In the “detection” step, the JDPD gets in touch with the input tone to be detected. The device’s wave function oscillates around the potential minimum following the stimulus. The “digitalization” is accomplished by flux-switching the JDPD in the double-well configuration. The wave function will collapse in the left $|L\rangle$ or right state $|R\rangle$ depending on the phase displacement of the input tone. In the “sense” step, we probe the JDPD to gather information on the wave function’s final state.

displacement θ_r :

$$I(t) = I_0 \sin(\omega_r t + \theta_r). \quad (8)$$

The wave function is described by a coherent state, in which the expectation value of φ follows the input tone's time evolution:

$$\langle \varphi \rangle(t) = \varphi_0 \sin(\omega_r t + \theta_0), \quad (9)$$

where, in general, φ_0 and θ_0 depend on the $I(t)$ parameters. For instance, in the case in which $\omega_r < \omega_0$, φ_0 and θ_0 take the values

$$\varphi_0 \approx 2\pi \frac{LI_0}{\Phi_0}, \quad (10)$$

$$\theta_0 \approx \theta_r, \quad (11)$$

which means that the information on the input tone displacement θ_r is transferred to θ_0 .

According to the quantum-mechanical evolution of a coherent state, the wave function's standard deviation [34] is constant in time and it is equal to

$$\sigma = 2e\sqrt{\frac{2Z_0}{\hbar}}, \quad (12)$$

where $Z_0 = \sqrt{L/C}$ is the characteristic impedance of the LC resonator.

The “digitalization” step shown in Fig. 2 is accomplished by diabatic flux-switching the JDPD to a bistable potential configuration ($\phi_+ = \pi/2 \rightarrow \phi_+ = \pi$). Intuitively, according to the sign of $\langle \varphi \rangle$ at the flux-switching time t_1 , the wave function of the system will primarily be confined in either of the two wells, depending on the initial phase θ_r imposed onto the coherent state by the input current $I(t)$. We define these two states as $|L\rangle$ and $|R\rangle$, associated with the wave function collapsing in the left or right well of the potential energy.

Right after, $I(t)$ is turned off to prevent further dynamics of the wave function after the “digitalization” is completed. A detailed explanation of how the probability of confining the wave function in one of the two wells depends on θ_r can be found in the section on numerical analysis (Sec. IV). The position of the phase particle can now be “sensed,” as the two possible outcomes of a measurement of the φ operator will have opposite values, which correspond to opposite signs for the current flowing through the central inductor L , according to

$$\langle I \rangle = \frac{\Phi_0}{2\pi L} \langle \varphi \rangle. \quad (13)$$

So far, we have explained how to map the initial phase θ_r of the input current $I(t)$ to the occupation probability of the

wave function of the JDPD in the bistable configuration. It is thus important to describe some details of the dynamics during the flux switch, which unveils the advantages of the JDPD protocol with respect to the one used in the JPM.

The primary difference lies in the fact that we do not require the JDPD to be in resonance with the input tone that we want to sense. This has the tremendous advantage that the emission spectrum in the bistable configuration can be designed to be far from the absorption spectrum of any nearby circuit. Therefore, the emitted photons generated during the relaxation of the system during the “digitalization” step will likely not harm the coherence of the surrounding circuitry [15,35,36]. Moreover, the symmetric topology [37,38] of the JDPD suppresses the flux-induced backaction at the active node. As any real device is going to have asymmetries because of fabrication uncertainties, we also discuss in the Appendix how to correct for such imperfection by properly adjusting the differential flux ϕ_- before the protocol starts.

IV. NUMERICAL ANALYSIS

The timing diagram shown in Fig. 2 has been validated numerically using the Lindblad master equation solver *mesolve* implemented in QuTip [33]. These simulations allow us to derive key features of the JDPD phase detection protocol, such as the probabilities associated with the wave function's time evolution.

The general form of the Lindblad master equation is given by

$$\frac{d\rho}{dt} = -i[H, \rho] + \sum_k \left(L_k \rho L_k^\dagger - \frac{1}{2} \{L_k^\dagger L_k, \rho\} \right), \quad (14)$$

where ρ is the density matrix of the system, H is the Hamiltonian operator, and the L_k are the Lindblad operators [33,39–41]. To describe the time evolution of the JDPD's wave function, we have truncated the series in Eq. (14) at the first order and considered as Lindblad operator L_1 the quantity

$$L_1 = \sqrt{\gamma} a, \quad (15)$$

where γ is the dissipation rate and a is the annihilation operator, defined in Eq. (6), through which the environment couples to the system. This model corresponds to a relaxation map [39–41], which describes the JDPD's energy loss assuming the temperature of the system $T = 0$ [42].

Simulations have been carried out by considering a central inductor $L = 220$ pH and junctions with a critical current $I_c = 5.4$ μ A. These parameters come from the experimental realization of the JDPD, which will be discussed in more detail in the section (Sec. V). The values for L and I_c lead to $2\beta_L = 7$, following the definition in

Eq. (3). This means that the Josephson contribution to the total energy is large enough to guarantee the formation of a double-well potential, which is necessary to confine the wave function when a flux switch is applied. To model the capacitive contribution of the Josephson junctions, we have considered $2C = 78$ fF, which is the value expected from fabrication. The parameters introduced above provide $E_L = 743$ GHz, $E_J = 2682$ GHz, and $E_C = 0.28$ GHz, according to Eqs. (3) and (4). It is worth noting that the system is dominated by the Josephson and inductive contributions, which lead the wave function to be very narrowed with respect to the quantum-mechanical operator φ [43]. The contributions of energies lead to a frequency of $\omega_0/2\pi = 41$ GHz when the potential is in the harmonic shape and $\omega/2\pi = 112$ GHz when it is in the double-well configuration.

To model the dissipation in the presented device, the relaxation rate γ has been extracted from numerical analysis performed in PSCAN2 [44]. This simulator allows one to study the classical dynamics of the circuit and includes a solid model to describe the Josephson junctions based on the tunnel junction microscopic model [45–48]. The parameters required to model the Josephson junctions have been determined in agreement with the typical fabrication values. In particular, we have considered $I_c = 5.4$ μ A, gap voltage $V_g = 2.6$ mV, McCumber parameter [49] $\beta_C = 53$, ratio $I_c R_N / V_g = 0.8$, and normal-to-subgap resistance ratio [44] $R_n / R_{sg} = 0.1$. We have estimated $1/\gamma \simeq 7$ ps, which is comparable to dissipation rates reported in the literature for similar standalone QFP devices [29,50,51]. It is worth noting that, in future design, this value can be properly adjusted by changing the capacitance C or the effective resistance R of the junctions. We can also increase the β factor, associated with the barrier height, to reduce the effect of dissipation on the phase trapping.

Simulations have been carried out by considering a sinusoidal input tone with a frequency of 7 GHz modulated by a Gaussian envelope with standard deviation of 100 ps. The input tone frequency sets the time scale for the flux switch. Intuitively, the barrier height that separates the two wells should rise faster than the oscillations induced by the input tone, to prevent the redistribution of the probability between the two possible states. In the case of our simulations, we assume that the duration of the flux switch t_{flip} is equal to 50 ps corresponding to a 20 GHz tone in the frequency domain. This value comes from the fact that our future idea is to provide the flux-switch signal with an integrated SFQ circuit, and a 20 GHz clock has been proposed to be optimal in this type of superconducting device [22].

The amplitude of the input stimulus is expressed in terms of the wave function's maximum elongation:

$$\varphi_0 = 2\pi L I_0 / \Phi_0. \quad (16)$$

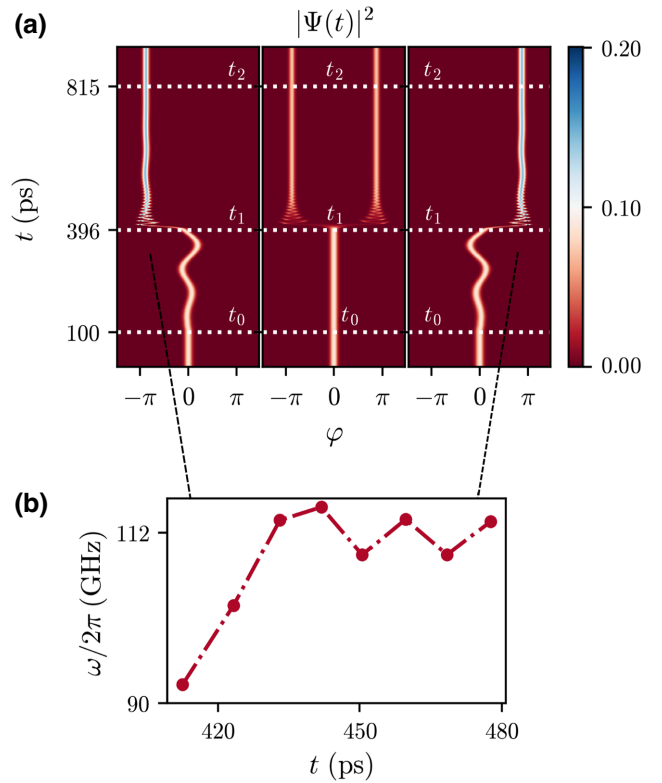


FIG. 3. Simulations of JDPD with QuTip [33]. (a) The JDPD's wave function has been simulated according to the timing diagram reported in Fig. 2. In the left part, an initial displacement $\theta_r = 0$ has been considered for the sinusoidal input tone. As a consequence, the wave function collapses in the left well after the flux-switch tone. The same sequence has been simulated in the right part but with an initial displacement $\theta_r = \pi$ of the input tone. In this case, the wave function falls in the right well. The central part refers to the case in which the input tone is not applied. When at $t = t_1$ the potential is flipped in its double-well configuration, the wave function is split in half and we have an equal probability of measuring it in the left and right wells. (b) While falling in the well, the JDPD's wave function performs damped nonharmonic oscillations, which lead to a gradual increase of the frequency.

In the case of simulation in Fig. 3, we have chosen

$$\varphi_0 = 2\sigma, \quad (17)$$

where σ is the standard deviation of the JDPD's wave function, according to Eq. (12). This value is found to be optimal to achieve high fidelity, as shown in Fig. 4(b), where we will address phase detection performed with other values of the stimulus's amplitude.

The wave function's time evolution is reported in Fig. 3(a). The system is initialized in the harmonic state and the wave function is expected to collapse in the ground state of the potential, corresponding to the "ready" step in Fig. 2. At $t = t_0$, the input signal starts to drive the wave function around the minimum. In the simulations, the

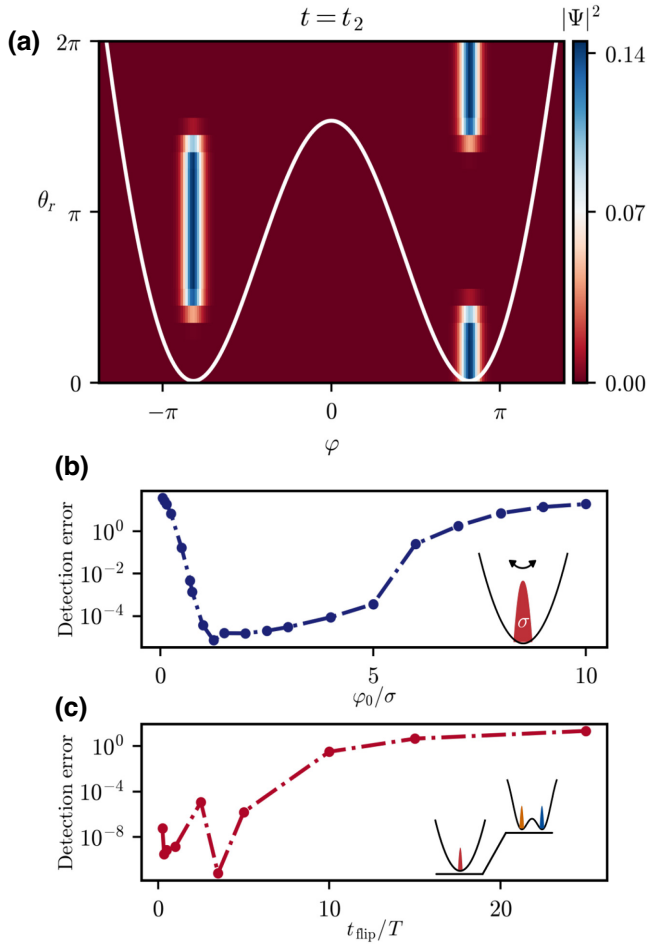


FIG. 4. (a) JDPD's probability distribution $|\Psi(t)|^2(t)$ at $t = t_2$ as a function of the initial displacement θ_r of the input tone. (b) Detection error as a function of the wave function's maximum elongation φ_0 during the driven harmonic motion; φ_0 is expressed in units of the wave function's rms σ . (c) Detection error as a function of the flux-switch rise time t_{flip} normalized in terms of the input signal's period T .

sinusoidal waveform has a duration of five periods, which corresponds to 715 ps for a frequency of 7 GHz. Driven coherently by the external tone, the JDPD's wave function is described by a Gaussian wave packet, in which the mean value $\langle\varphi(t)\rangle$ evolves as

$$\langle\varphi\rangle = \varphi_0 \sin(\omega t + \theta_0), \quad (18)$$

where $\omega/2\pi = 7$ GHz and θ_0 is the displacement of the sinusoidal input signal. As discussed in the section on the principle of operation (Sec. III), the wave function's standard deviation depends on device parameters and it is constant during the driven evolution. According to Eq. (12), we have estimated $\sigma = 0.31$ rad considering the values of L and C indicated above. Discrimination between the two states is made at $t = t_1$ when the flux switch is applied. In simulations, t_1 is chosen to center the flux

switch with respect to the beginning and the end of the input tone. The wave function collapses in either the left $|L\rangle$ or right $|R\rangle$ state depending on the initial displacement θ_r . For instance, the left part of Fig. 3(a) shows the wave function's evolution considering an initial $\theta_r = 0$, which leads the wave function to fall in the left well after the flux-switch pulse. In the right part of Fig. 3(a), the opposite situation is represented, corresponding to $\theta_r = \pi$. The central part refers to the case in which the input tone is not applied. When at $t = t_1$ the potential is flipped in its double-well configuration, the wave function is split in half and we have an equal probability of measuring it in the left and right wells.

While collapsing in the well, one may ask which is the induced backaction on the input signal's source. In this transient, the JDPD can be modeled as an effective voltage source V_j that can generate a disturbing signal on the rest of the circuit [15]. According to the ac Josephson relation [49,52], the produced backaction signal is proportional to the time derivative of $\langle\dot{\varphi}(t)\rangle$. After the flux switches, the JDPD's wave form performs a damped non-harmonic motion, where the oscillations frequency gradually increases [35,36]. Since phase detection does not require the JDPD to be in resonance with the input signal source, one can design the detector in such a manner that these oscillations are outside the source's absorbing spectrum, preventing backaction being induced on the system. For example, considering the selected parameters for simulations, these oscillations have frequencies above 90 GHz, as shown in Fig. 3(b). They stabilize around 112 GHz, which corresponds to the frequency of the two wells when the potential is set in the flipped configuration (i.e., $\phi_+ = \pi$).

The sequence is completed at $t = t_2$ when the position of the phase particle can be "sensed," as the two possible outcomes of a measurement of the φ operator will have opposite values, which correspond to opposite signs for the current flowing through the central inductor L :

$$\langle I \rangle = \frac{\Phi_0}{2\pi L} \langle \varphi \rangle. \quad (19)$$

Figure 4(a) exhibits the wave function's probability density $|\Psi|^2$ at $t = t_2$ for several values of the input tone's displacement θ_r . According to these simulations, a fidelity close to 1 is in principle achievable; however, this estimation depends on several parameters. Figure 4(b) shows the detection error as a function of the wave function's maximum elongation φ_0 in units of the wave function's standard deviation σ :

$$\varphi_0 \equiv n\sigma. \quad (20)$$

Fidelity is maximized when $n \in [1, 6]$. Values below this range correspond to small oscillations around $\varphi = 0$. As

a consequence, when the flux switch is applied, the wave function is split between the two wells, leading to a reduction in measured fidelity. When $n > 6$, the barrier height is not large enough to confine the wave function, and this leads to a redistribution of probability.

Another factor that limits fidelity is the flux-switch duration t_{flip} . According to the simulations in Fig. 4(c), a fidelity close to 1 is achievable when $t_{\text{flip}} < 10T$, where $T = 2\pi/\omega$ and $\omega/2\pi = 7$ GHz is the simulated frequency for the input tone. In fact, a slow rise time for the barrier height induces a redistribution of probability between the two wells at each input tone's period. Considering the typical frequencies for superconducting resonators, optimal values for t_{flip} are in the order of hundreds of picoseconds. We want to point out that the possibility to manipulate the potential shape diabatically has already been exploited both experimentally and theoretically in Refs. [30–32]. These papers demonstrated coherent oscillations of a tunable superconducting flux qubit by manipulating its energy potential with nanosecond-long pulses of magnetic flux. Given the resemblance between the JDPD and the device reported in Refs. [30–32], we can argue that fast potential manipulation can be performed also in the case of the presented detector.

A possible approach to generate pulses with hundreds of picoseconds rise time involves the use of a dedicated SFQ flux generator, which can operate with a clock of tens of gigahertz [16,22]. Another benefit of the use of high-speed SFQ circuitry lies in the possibility of performing multiple measurements on the same cycle, thus allowing averaging to reduce the noise contribution and improve fidelity. This is shown in Fig. 5, where the measurement sequence with multiple flux flips has been simulated in QuTip.

A more detailed discussion about the integration of the JDPD with an SFQ-based platform can be found in the outlook section of this paper (Sec. VII).

V. DEVICE DESIGN AND EXPERIMENTAL SETUP

The JDPD has been realized in collaboration with SEEQC [53] using their multilayer fabrication process. The device micrograph is reported in Fig. 6(b). The JDPD central inductor L has been realized by a 40- μm -long and 1.4- μm -wide wire fabricated using a high-kinetic-inductance layer in NbN, with a total value of $L = 220$ pH. The rest of the circuit is made with conventional layers in Nb, characterized by smaller values of sheet inductance. The Josephson junctions are realized with a trilayer stack of Nb/ AlO_x /Nb with 1 kA cm^{-2} critical current density. In particular, we have chosen a Josephson junction with an I_c of 5.4 μA , corresponding to $2\beta_L = 7$. As discussed in the section on the device model (Sec. II), this value is large enough to produce a double-well potential when the device is flux-switched.

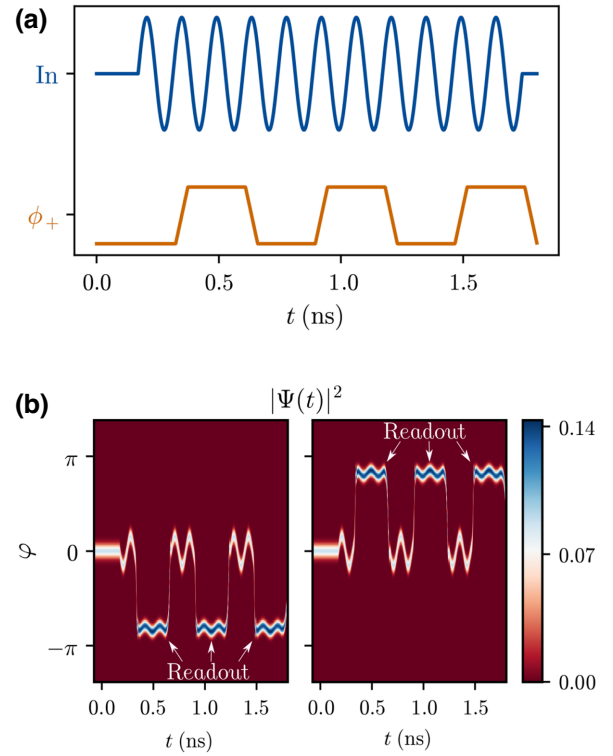


FIG. 5. Multiple phase detections are performed on the same sinusoidal input tone. (a) Time diagram of the applied signals. The flux-switch curve is orange, while the sinusoidal input tone is blue. (b) The time sequence reported in (a) has been simulated in QuTip and the $|\Psi(t)|^2$ is shown. In particular, in the left part, the sinusoidal input tone is initialized with displacement $\theta_0 = 0$ while in the right one $\theta_0 = \pi$.

The JDPD is equipped with two dc lines, DC1 and DC2, and an rf line, which allow us to have precise control of the magnetic fluxes threading the device's loops. The rf line is designed to pass under the JDPD main loop, as shown in Figs. 6(a) and 6(b). Considering its geometry, the rf line forces the current to circulate around the JDPD main loop without flowing through the central inductor L , which contributes only to the common flux ϕ_+ . The flux ϕ_+ allows us to set and reset the JDPD, changing the potential from a harmonic configuration to a double-well one and vice versa. According to simulations reported in the numerical analysis section (Sec. IV), these operations should be performed diabatically to enhance the detection fidelity and the protocol speed. For this reason, we have connected the rf line below the JDPD loop to a conventional 50 Ω coplanar waveguide (CPW) to preserve as much as possible the shape of the flux switch. The CPW is made of an 11- μm -wide superconducting core in Nb and it has a gap of 7 μm to ground.

The lines DC1 and DC2 provide individually a contribution in both the JDPD meshes. To be more clear, defining I_{DC1} and I_{DC2} as the currents flowing respectively in DC1

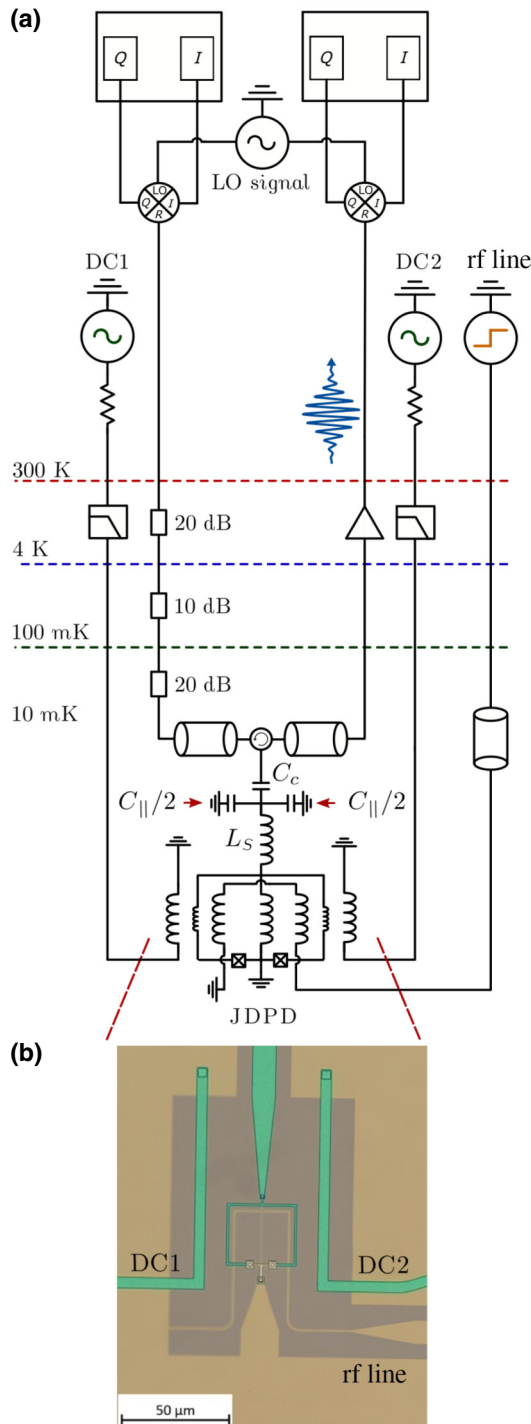


FIG. 6. (a) Measurement setup for the characterization of the JDPD. The device has been measured in reflection through the standard heterodyne detection technique. The JDPD acts like a flux-tunable inductance, which changes the resonance frequency as a function of the applied flux ϕ_+ . These two fluxes act differently on the JDPD's potential, producing a flip or controlling the asymmetries with respect to $\varphi = 0$. The magnetic flux is provided by an rf flux line and two independent dc flux lines connected to two arbitrary wave-form generators (AWGs) at room temperature. (b) Optical microscope image of one of the realized devices.

and DC2, we have

$$\begin{aligned}\phi_1 \frac{\Phi_0}{2\pi} &= M_{1,1} I_{DC1} + M_{1,2} I_{DC2}, \\ \phi_2 \frac{\Phi_0}{2\pi} &= M_{2,1} I_{DC1} + M_{2,2} I_{DC2},\end{aligned}\quad (21)$$

where $M_{i,j}$ is the mutual inductance between the dc line j and the mesh i . As shown in Fig. 6(b), the two dc lines are placed on opposite sides with respect to the central inductor L , which indicates that the matrix of coefficients $M_{i,j}$ is

$$\begin{aligned}M_{1,1} &= -M_{2,2} = M_{\text{dir}}, \\ M_{1,2} &= -M_{2,1} = M_{\text{opp}}.\end{aligned}\quad (22)$$

According to Eqs. (22), any combination of ϕ_+ and ϕ_- can be generated by properly biasing the two dc lines. Cases of particular interest occur when $\phi_+ = 0$, which implies $I_{DC1} = I_{DC2}$,

$$\begin{aligned}0 &= \frac{\phi_1 + \phi_2}{2} \frac{\Phi_0}{2\pi} = \frac{M_{\text{dir}}}{2} (I_{DC1} - I_{DC2}) \\ &+ \frac{M_{\text{opp}}}{2} (I_{DC1} - I_{DC2}) \implies I_{DC1} = I_{DC2},\end{aligned}\quad (23)$$

and when $\phi_- = 0$, leading to $I_{DC1} = -I_{DC2}$,

$$\begin{aligned}0 &= \frac{\phi_1 - \phi_2}{2} \frac{\Phi_0}{2\pi} = \frac{M_{\text{dir}}}{2} (I_{DC1} + I_{DC2}) \\ &+ \frac{M_{\text{opp}}}{2} (I_{DC1} + I_{DC2}) \implies I_{DC1} = -I_{DC2}.\end{aligned}\quad (24)$$

The two dc lines are employed to control the asymmetries of the system and to set the JDPD working point. The dc lines are realized with a 5- μm -wide wire in Nb. Both rf and dc lines are connected at room temperature to an AWG with a 1 GS/s sampling rate.

The JDPD dynamics is investigated through reflection measurements by adopting a typical heterodyne detection setup as indicated in Fig. 6(a). To shift the resonance frequency in the measurable range [4 GHz, 8 GHz], a lumped LC resonator has been coupled to the device. The circuit comprises an inductor L_s in series with the JDPD and a parallel-plate capacitor C_{\parallel} close to the ground. A coupling capacitor C_c connects this resonator to the external experimental apparatus, as shown in Fig. 6(a). At linear order of approximation, the JDPD works as a lumped variable inductance L_{JDPD} , which depends on ϕ_+ and ϕ_- :

$$L_{\text{JDPD}}(\phi_+, \phi_-) = \left(\frac{\Phi_0}{2\pi}\right)^2 \frac{1}{d^2 U(\varphi)(\phi_+, \phi_-)/d\varphi^2|_{\varphi_{\min}}},\quad (25)$$

where φ_{\min} is the potential energy minimum where the phase particle is trapped. In this way, the system is characterised by a resonance frequency,

$$\frac{\omega}{2\pi} = \frac{1}{\sqrt{(C_c + C_{\parallel})(L_{\text{JDPD}} + L_s)}}, \quad (26)$$

which is directly linked to the JDPD state.

The values of L_s , C_c , and C_{\parallel} have been carefully chosen to deliver signals out of resonance through the JDPD input node, as requested by the phase detection technique while preserving the resonance visibility. These constraints lead us to consider $L_s = 300$ pH, $C_c = 100$ fF, and $C_{\parallel} = 1.4$ pF, determined in agreement with numerical simulations. The capacitors C_c and C_{\parallel} have been realized in a parallel-plate configuration between two Nb layers separated by a dielectric part in SiO_2 , characterized by a specific capacitance of 0.44 fF/ μm^2 . This choice is obligatory since it is not possible to achieve large values of capacitance with interdigitated capacitors, as required in the present circuit. The drawback is that the typology of capacitors leads to higher values of the circuit internal losses [14,15], and they are more prone to spread in manufacturing parameters.

The inductor L_s is realized using a high-kinetic-inductance layer in NbN, which results in a large value of L_s in a relatively small portion of space. The measurements were performed at about 10 mK using a dry dilution refrigerator.

VI. EXPERIMENTAL RESULTS

Device characterization starts by performing spectroscopy versus fluxes ϕ_+ and ϕ_- . Comparing the resulting map with simulations, we can determine the locations of the bias points corresponding to the potential energy configurations that the JDPD can assume during the protocol. We have measured a resonance frequency of 6.6 GHz when the JDPD is set in the state $\phi_+ = 0$, 6.4 GHz when the JDPD is in the harmonic configuration, and 6.588 GHz for $\phi_+ = \pi$. In the harmonic state, we have estimated a resonator quality factor $Q_{\text{int}} \simeq 70$, corresponding to a decay rate of $\kappa = 1/(0.22 \text{ ns})$.

Phase detection requires the determination of the symmetry point θ_{symm} concerning the flux ϕ_- . As suggested by the name, θ_{symm} is the value of ϕ_- that leads to an equal splitting of the wave function in the two wells when a flux switch is applied in the absence of any external input signal. Theoretically, θ_{symm} should correspond to $\phi_- = 0$; however, some factors, such as asymmetric junctions or fabrication spread, could lead to $\theta_{\text{symm}} \neq 0$, as discussed in the Appendix. The determination of θ_{symm} is crucial in order to achieve state-independent fidelity. Once we have calibrated the system, we have evaluated experimentally the JDPD's capability to work as a phase detector, according to the time sequence reported in Fig. 7(A).

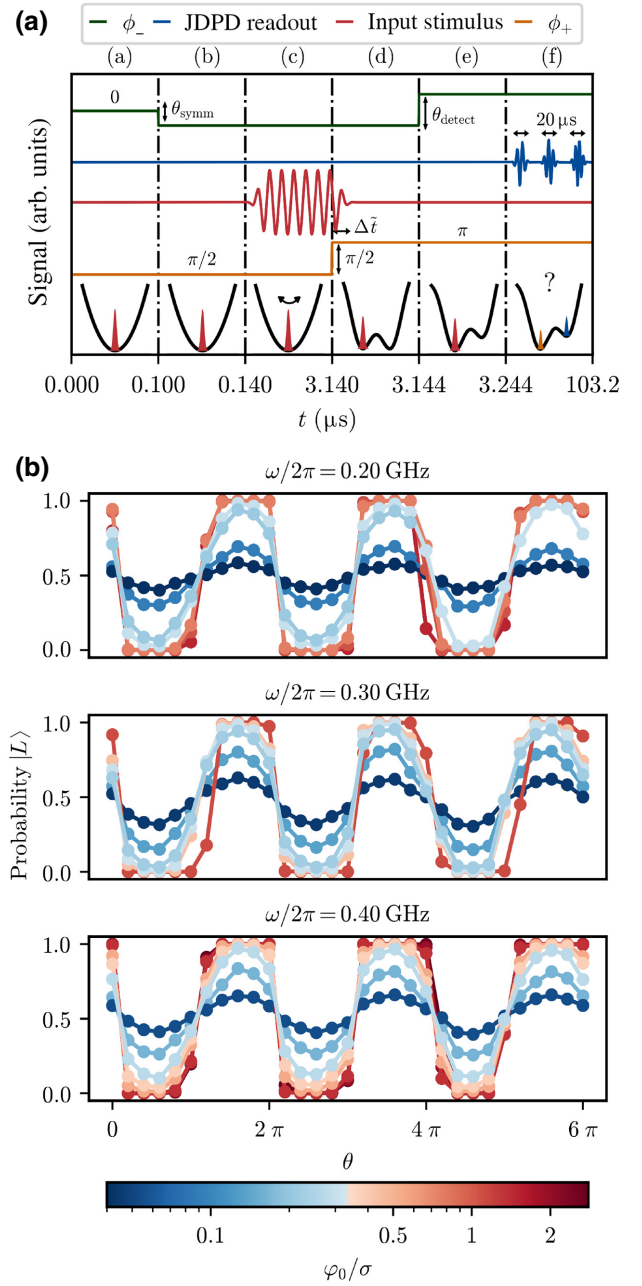


FIG. 7. (A) Time sequence performed experimentally to demonstrate phase detection, as described in detail in the text. (B) Phase detection has been performed for different values of input frequency and amplitude expressed in terms of φ_0/σ , as introduced in the numerical analysis section (Sec. IV). Results are compatible with the theoretical expectations and demonstrate the feasibility of the JDPD approach.

Phase detection begins by preparing the system in the harmonic configuration. We wait for a cooldown time of 100 ns to ensure that the wave function collapses in the minimum of the potential energy. This step forces the device to “reset” in the ground state and makes it ready to be flipped in the double-well configuration. At $t = 100$

ns, we apply $\phi_- = \theta_{\text{symm}}$, determined during the calibration. In step (c) of Fig. 7(A), the JDPD is driven by an input stimulus for a total duration of 3 μs . The application of this tone makes the wave function oscillate coherently around the potential minimum, as expected from Eq. (18). The potential is flipped in the double-well configuration at 3.140 μs , as indicated in step (d) in Fig. 7(A). The flux switch is provided diabatically, with a rise time of 1 ns corresponding to the maximum achievable by AWGs. The effect of the potential flipping makes the wave function collapse in the left $|L\rangle$ or $|R\rangle$ state, depending on its position with respect to $\varphi = 0$ when the flux switch is applied. To ensure the overlap between the pulses, we retarded the end of the stimulus by $\Delta\tilde{t} = 4$ ns with respect to the beginning of the flux switch.

The readout of the JDPD state is accomplished in steps (e) and (f) in Fig. 7(A). In the actual chip design, there is no possibility of measuring the superconducting current that passes through the inductor L and the JDPD's readout is performed by using the spectroscopy measurement. However, in the symmetric condition, when left $|L\rangle$ and $|R\rangle$ states are equiprobable, the two wells have the same resonance frequency and it is tricky to distinguish them.

To overcome this difficulty, we can unbalance a little bit the frequency of the two states by applying $\phi_- = \theta_{\text{detect}}$. Reasonably, θ_{detect} should be small enough not to perturb the system too much. In the case of measurement, we have chosen $\theta_{\text{detect}} = 0.2$ rad, which has proven experimentally to be a good value for the observability of the $|L\rangle$ and $|R\rangle$ states. The JDPD is, then, measured in reflection at five probing frequencies; each readout pulse has a length of 20 μs corresponding to 100 μs of total duration for step (f) in Fig. 7(A).

The sequence described above is repeated 5000 times to obtain statistics on the trapping probability. As illustrated in Fig. 7(B), the detection sequence has a total duration of several microseconds, primarily due to step (f) in Fig. 7(A), where we measure the JDPD state in reflection. However, in future layouts, we will probe the device state by digitalizing the sign of the current flowing through the inductor L . This task can be efficiently performed by an SFQ current comparator, which can operate at tens of gigahertz clock speed [19,22], bringing important benefits to reduce the duration of step (f). Furthermore, step (e) in Fig. 7(A), in which the device frequency is unbalanced, is no longer required and $\phi_- = \theta_{\text{symm}}$ can be set at the beginning of the calibration and left untouched during the sequence. Since detection will not be performed by measuring the JDPD resonance frequency, we can opportunely modify the parameters of the resonator coupled to the device to minimize the input stimulus's ringing time and, consequently, the duration of step (c) in Fig. 7(A). From these arguments, we conclude that the timing reported in Fig. 7(B) can be extremely reduced to a few nanoseconds time scale, as theoretically predicted in Fig. 3(a).

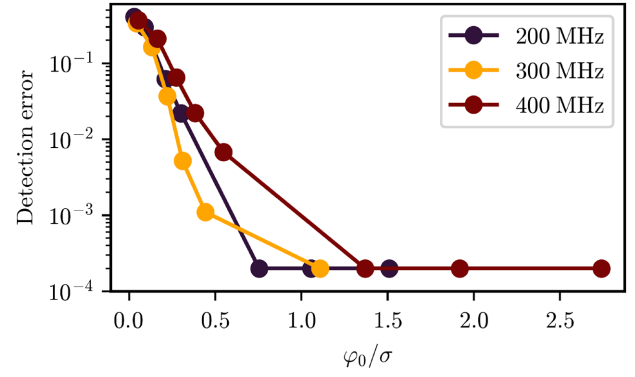


FIG. 8. Detection error versus the input tone amplitude, expressed in terms of φ_0/σ . Results are compatible with theoretical predictions reported in Fig. 4(b).

Experimental outcomes are reported in Fig. 7(B). The detection protocol has been performed by changing the stimulus initial phase θ in the range $\theta \in [0, 6\pi]$ for different values of input frequency up to 400 MHz, which is the maximum tone frequency that our instruments can generate with a controlled input phase. We have also swept over the amplitudes A_m , expressed in terms of φ_0/σ .

Results show that JDPD is sensitive to the applied input tone. In particular, when the amplitude A_m is large enough, as in the case of $\varphi_0/\sigma > 0.55$, the device is able to perform the digitalization of stimulus phase θ , as this information is mapped into the wave function's collapsing probability in either of the two states $|R\rangle$ and $|L\rangle$. The gray zone reasonably decreases with the amplitude A_m until, in the case of small input amplitudes, the wave function is no longer capable of reaching the $|L\rangle$ and $|R\rangle$ states with probability approaching 1. In this case, the interpolation of points of Probability $|L\rangle$ vs θ exhibits a sinusoidal shape compatible with the input tone profile. When A_m increases, the effect of digitalization leads to a “clipping” of the interpolation shape, which is more evident for the red points in Fig. 7(B). This behavior is compatible with the theoretical prediction reported in Fig. 4(a), where the wave-function probability distribution $|\Psi(t)|^2$ is reported as a function of the initial displacement θ . Figure 8 shows the dependence of the detection error on the stimulus amplitude A_m . According to experimental outcomes, phase detection can be achieved with fidelity of 99.98%, in a similar way compared to numerical analysis in Fig. 4(b).

VII. OUTLOOK

In this work, we have illustrated a phase detection technique based on a Josephson digital phase detector (JDPD). Simulations and experimental outcomes show that digitalization can reach fidelities close to 1 in a nanosecond time

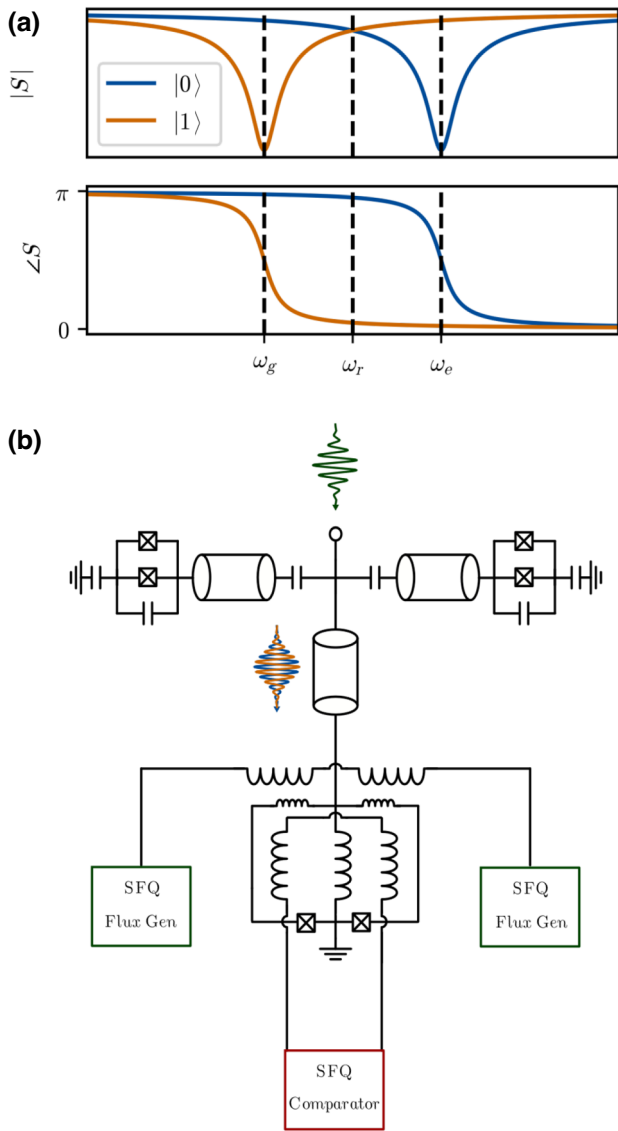


FIG. 9. (a) Parameters S measured in a typical superconducting qubit readout scheme. A shift of the resonance frequency is observed depending on the qubit's state, which is visible in both amplitude $|S|$ and phase $\angle S$. To exploit the JDPD detection technique, we need to maximize the separation between the state $|0\rangle$ and $|1\rangle$ in phase. This operation can be done by probing the cavity at the resonator bare frequency, i.e., $\omega = \omega_r$. (b) Possible experimental setup to measure the qubit's state involving the JDPD. In this sketch, two resonator-qubit systems are capacitively coupled to a feedline connected inductively to a JDPD device. The detector's states are tuned by an SFQ flux generator and the measurement output is digitalized by using an SFQ comparator.

scale with negligible backaction on the source. These characteristics make the JDPD approach particularly suitable for the readout of superconducting qubits.

A typical scheme for superconducting qubit measurement exploits high- Q resonators whose bare

resonant frequency ω_R is shifted by a factor χ , depending on the state of a dispersively coupled qubit. Discrimination can be performed by probing the resonator with microwave tones and measuring the response in phase and amplitude, as reported in Fig. 9(a). A similar approach can be pursued in the case of the presented detection technique, as schematized in Fig. 9(b). We can probe the cavity by sending a tone at $\omega = \omega_r$ to be maximally sensitive to the phase response of the dressed resonator. Subsequently, the output signal can be sent to an inductively coupled JDPD set to be in the “ready” state. The JDPD will behave almost as a purely inductive element at input frequency ω_r , so $\varphi(t)$ will be phase-locked to the current injected by the readout tone.

The operations needed to drive and measure the JDPD can be performed by an SFQ circuitry [17,18]. These devices store the bits of information using propagating fluxons, as picosecond voltage pulses whose time integral equals the superconducting flux quantum $\Phi_0 = h/2e$. Thanks to their very low power dissipation, energy-efficient SFQ (ERSFQ, eSFQ) circuits [54–56] could be safely located contiguously to the quantum chips, and they offer the possibility to operate at very high speeds (tens of gigahertz clock) with small jitter [21]. Therefore, an SFQ circuitry can grant the required phase locking between the input pulse and flip pulse, making the detection possible with fidelities close to 1.

To realize the discussed system, we are currently testing an optimized JDPD and designing a complete circuit, which includes an SFQ flux generator [21], to rapidly flux-switch the potential, and an SFQ comparator [24,57–59], to measure the JDPD state.

VIII. CONCLUSIONS

In conclusion, we have reported a phase detection technique based on a Josephson digital phase detector. This device is based on a QFP and has a tunable potential which can be diabatically switched from a single-minimum potential to a double-minima configuration. If a coherent signal is applied, the system wave function collapses in either of its two degenerate wells depending on the phase sign of the input tone. This information is therefore mapped in the current direction flowing in the JDPD central linear inductor. The proposed measurement scheme is performed directly on-chip at the millikelvin stage of a dilution refrigerator. Furthermore, it eliminates the need for microwave output lines, which brings significant technical and economic challenges to system scaling. The JDPD works far detuned with respect to the qubit, thus reducing the effects of backaction. The basic concepts behind this detection scheme have been experimentally verified. The capability to work as a phase detector has also been demonstrated up to 400 MHz tone, with a

remarkable agreement between the experimental outcomes and simulations.

As a future perspective, we have discussed a possible implementation of this device to read out the state of a superconducting qubit, which can be accomplished by properly adjusting the JDPD design parameters. This detector is also well suited to work with a scalable SFQ architecture, which can be employed to drive and measure the JDPD state. Therefore, we envision the JDPD as part of a more complex architecture, in which the classical qubit control, measurement, and data processing are performed by a classical SFQ processor. This approach can be a valid solution to enhance the scalability of superconducting quantum systems [16,22], which remains a big engineering challenge to realize practical error-corrected quantum computers [60].

ACKNOWLEDGMENTS

The authors would like to thank D. Yohannes, J. Vivalda, M. Renzullo, and A. Chambal-Jacobs for the fabrication of the samples, and A. Kirichenko, A. Salim, and R. Albu for advice in design.

The work was supported by the project ‘‘On-chip signal generation for superconducting quantum processors (SFQ4QPU)’’, in the frame of Eurostars CoD 15 Call 2021; the project ‘‘SQUAD – On-chip control and advanced read-out for superconducting qubit arrays (SQUAD)’’ in the frame of Programme STAR Plus, financially supported by UniNA and Compagnia di San Paolo; and the project ‘‘Superconducting quantum-classical linked computing systems (SuperLink)’’, in the frame of QUANTERA2 ERANET COFUND in Quantum Technologies.

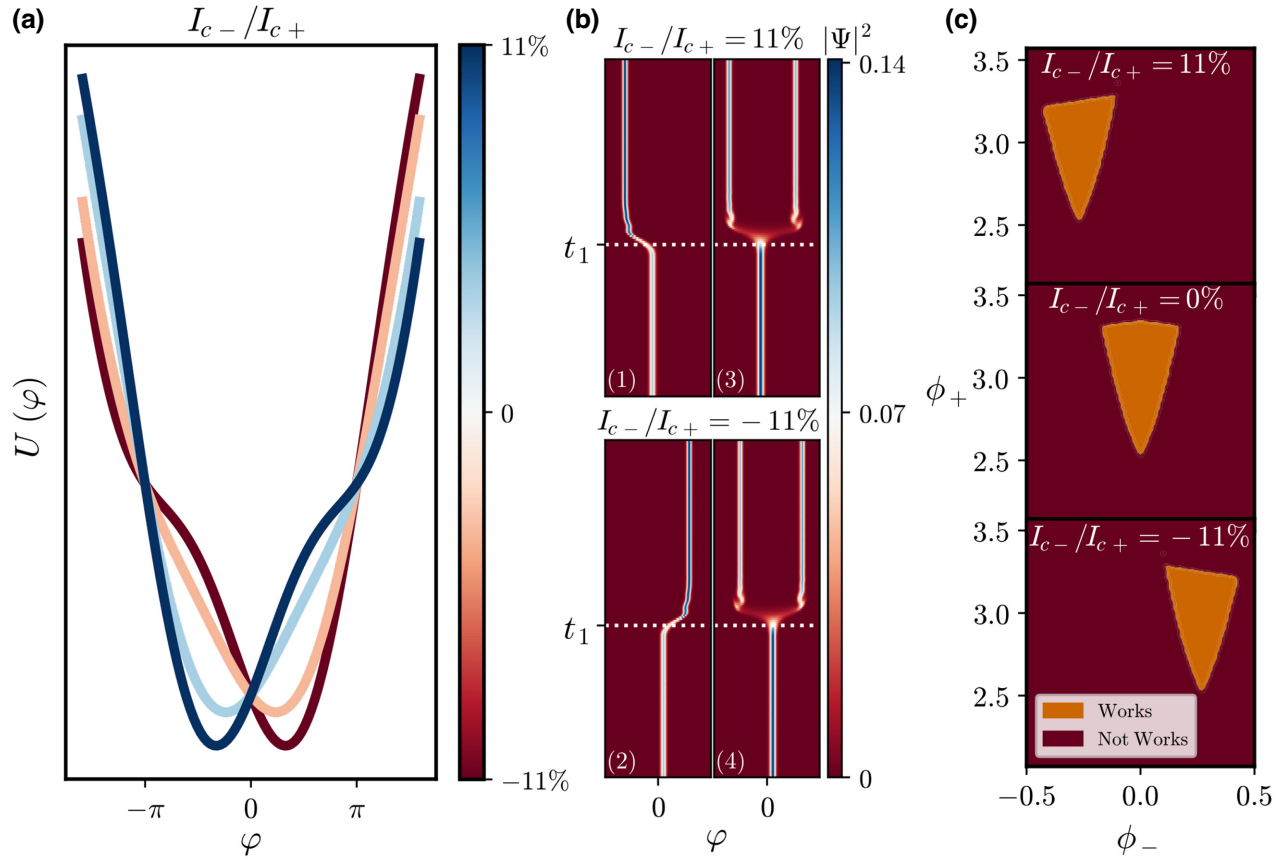


FIG. 10. (a) JDPD’s potential shape when $\phi_+ = \pi/2$ and $\phi_- = 0$ for several values of the ratio I_{c+}/I_{c-} . The presence of asymmetries leads to a shift in the potential minimum and the wave function acquires an offset with respect to $\varphi = 0$. (b) In parts (1) and (2), in the absence of external input, an applied flux switch makes the wave function collapse in the two wells with different probabilities. In this QuTip simulation performed with $I_{c+} = 9 \mu\text{A}$ and $I_{c+}/I_{c-} = \pm 11\%$, we have 99.999% of the probability of reaching the left (1) and right well (2). In parts (3) and (4), however, state-independent fidelity can be achieved by adjusting the value of ϕ_- to $\phi_- \simeq 0.46$ rad. (c) The numerical analysis performed with QuTip is supported by classical simulations made in PSCAN2 [44]. Sweeping on ϕ_+ and ϕ_- , we have determined regions in which the JDPD is capable of correctly performing phase detection. Simulations have been carried out considering the same parameters as adopted for QuTip, i.e., $I_{c+} = 9 \mu\text{A}$ and $I_{c+}/I_{c-} = \pm 11\%$. In particular, the top part refers to the case in which $I_{c+}/I_{c-} = +11\%$, the central part corresponds to perfect symmetrical JDPD, and the bottom part shows the condition when $I_{c+}/I_{c-} = -11\%$.

The research activities were also supported by the PNRR MUR project PE0000023-NQSTI and the PNRR MUR project CN_0000013—ICSC.

APPENDIX

A perfectly symmetrical JDPD is a fundamental requirement to obtain state-independent fidelity and guarantee the working condition of the detector.

However, in a real device, the JDPD will likely deviate from being perfectly symmetric due to various factors but mainly by parameter spread of the fabrication process and different flux trapped in the two JDPD branches.

In the case of an asymmetrical device, the potential energy becomes

$$U(\varphi) = \frac{1}{2L} \left[\left(\frac{\Phi_0}{2\pi} \right)^2 \varphi^2 - \frac{\Phi_0}{2\pi} (I_{c+} \cos(\phi_+) \cos(\varphi + \phi_-) - I_{c-} \sin(\phi_+) \cos(\varphi + \phi_-)) \right], \quad (\text{A1})$$

where the variables I_{c+} and I_{c-} have been introduced:

$$\begin{aligned} I_{c+} &= I_{c1} + I_{c2}, \\ I_{c-} &= I_{c1} - I_{c2}. \end{aligned}$$

Note that when the Josephson critical currents I_{c1} and I_{c2} are equal, $I_{c-} = 0$ and Eq. (3) is retrieved.

Figure 10(a) shows the potential shape for $\phi_+ = \pi/2$, $\phi_- = 0$, and several values of $I_{c-} \in [-1, 1] \mu\text{A}$. The presence of $I_{c-} \neq 0$ leads to a shift in the potential minimum and, consequently, the wave function acquires an offset with respect to $\varphi = 0$ in the absence of the external input tone. If a flux switch is applied, the wave function is distributed mostly in the well located on the same wave function side with respect to $\varphi = 0$. This makes the fidelity state-dependent and worsens the detector performance.

The protocol described above has been simulated with QuTip [33] in Fig. 10(b) parts (1) and (2). The numerical analysis has been performed by considering $I_{c+} = 9 \mu\text{A}$ and $I_{c+}/I_{c-} = \pm 11\%$, corresponding to a variation of 20% in the critical current value, which is generally larger than the typical fabrication spread. In both simulations, the potential is flipped at $t = t_1$ and the wave function collapses always in the same well with a probability of 99.999%. However, state-independent fidelity can be achieved by adjusting the value of ϕ_- . This is shown in Fig. 10 parts (3) and (4), where, in the same conditions of simulations as reported in Fig. 10(b) parts (1) and (2), the state-independent probability has been restored by applying $\phi_m \simeq \pm 0.46$ rad.

The numerical analysis performed with QuTip is supported by classical simulations made in PSCAN2 [44] shown in Fig. 10(c). Sweeping on ϕ_+ and ϕ_- , we have specific regions in which the JDPD is capable of correctly

performing phase detection. Simulations have been carried out considering the same parameters as adopted for QuTip, i.e., $I_{c+} = 9 \mu\text{A}$ and $I_{c+}/I_{c-} = \pm 11\%$. In particular, the top part of Fig. 10(c) refers to the case in which $I_{c+}/I_{c-} = +11\%$, the central part corresponds to perfect symmetrical JDPD, and the bottom part shows the condition when $I_{c+}/I_{c-} = -11\%$.

These considerations demonstrate that the proposed detector is robust with respect to asymmetries that can be corrected by properly changing ϕ_+ and ϕ_- using dc biases.

-
- [1] R. Janish, V. Narayan, S. Rajendran, and P. Riggins, Axion production and detection with superconducting rf cavities, *Phys. Rev. D* **100**, 015036 (2019).
 - [2] D. Salmikov, P. Satunin, D. V. Kirpichnikov, and M. Fitkevich, Examining axion-like particles with superconducting radio-frequency cavity, *J. High Energy Phys.* **2021**, 1 (2021).
 - [3] A. Berlin, R. T. D’Agnolo, S. A. R. Ellis, C. Nantista, J. Neilson, P. Schuster, S. Tantawi, N. Toro, and K. Zhou, Axion dark matter detection by superconducting resonant frequency conversion, *J. High Energy Phys.* **2020**, 1 (2020).
 - [4] N. Tsuji, C. L. Ayala, N. Takeuchi, T. Ortlev, Y. Yamanashi, and N. Yoshikawa, Design and implementation of a 16-word by 1-bit register file using adiabatic quantum flux parametron logic, *IEEE Trans. Appl. Supercond.* **27**, 1 (2017).
 - [5] Xiu Gu, Anton Frisk Kockum, Adam Miranowicz, Yu-xi Liu, and Franco Nori, Microwave photonics with superconducting quantum circuits, *Phys. Rep.* **718–719**, 1 (2017).
 - [6] I. Siddiqi, R. Vijay, F. Pierre, C. M. Wilson, M. Metcalfe, C. Rigetti, L. Frunzio, and M. H. Devoret, Rf-Driven Josephson Bifurcation Amplifier for Quantum Measurement, *Phys. Rev. Lett.* **93**, 207002 (2004).
 - [7] F. Mallet, F. R. Ong, A. Palacios-Laloy, F. Nguyen, P. Bertet, D. Vion, and D. Esteve, Single-shot qubit readout in circuit quantum electrodynamics, *Nat. Phys.* **5**, 791 (2009).
 - [8] J. M. Martinis, Qubit metrology for building a fault-tolerant quantum computer, *npj Quantum Inf.* **1**, 1 (2015).
 - [9] Alexandre Blais, Arne L. Grimsmo, S. M. Girvin, and Andreas Wallraff, Circuit quantum electrodynamics, *Rev. Mod. Phys.* **93**, 025005 (2021).
 - [10] A. Blais, R.-S. Huang, A. Wallraff, S. M. Girvin, and R. J. Schoelkopf, Cavity quantum electrodynamics for superconducting electrical circuits: An architecture for quantum computation, *Phys. Rev. A* **69**, 062320 (2004).
 - [11] P. D. Nation, J. R. Johansson, M. P. Blencowe, and Franco Nori, Colloquium: Stimulating uncertainty: Amplifying the quantum vacuum with superconducting circuits, *Rev. Mod. Phys.* **84**, 1 (2012).
 - [12] J. Kelly, *et al.*, State preservation by repetitive error detection in a superconducting quantum circuit, *ArXiv:1411.7403* (2014).
 - [13] P. Krantz, A. Bengtsson, M. Simoen, S. Gustavsson, V. Shumeiko, W. D. Oliver, C. M. Wilson, P. Delsing, and J. Bylander, Single-shot read-out of a superconducting qubit using a Josephson parametric oscillator, *Nat. Commun.* **7**, 1 (2016).

- [14] A. Opremcak, C. H. Liu, C. Wilen, K. Okubo, B. G. Christensen, D. Sank, T. C. White, A. Vainsencher, M. Giustina, A. Megrant, B. Burkett, B. L. T. Plourde, and R. McDermott, High-Fidelity Measurement of a Superconducting Qubit Using an On-Chip Microwave Photon Counter, *Phys. Rev. X* **11**, 011027 (2021).
- [15] A. Opremcak, I. V. Pechenezhskiy, C. Howington, B. G. Christensen, M. A. Beck, E. Leonard Jr., J. Suttle, C. Wilen, K. N. Nesterov, G. J. Ribeill, T. Thorbeck, F. Schlenker, M. G. Vavilov, B. L. T. Plourde, and R. McDermott, Measurement of a superconducting qubit with a microwave photon counter, *Science* **361**, 1239 (2018).
- [16] R. McDermott, M. G. Vavilov, B. L. T. Plourde, F. K. Wilhelm, P. J. Liebermann, O. A. Mukhanov, and T. A. Ohki, Quantum–classical interface based on single flux quantum digital logic, *Quantum Sci. Technol.* **3**, 024004 (2018).
- [17] O. Mukhanov, V. Semenov, and K. Likharev, Ultimate performance of the RSFQ logic circuits, *IEEE Trans. Magn.* **23**, 759 (1987).
- [18] K. Likharev and V. Semenov, RSFQ logic/memory family: A new Josephson-junction technology for sub-terahertz-clock-frequency digital systems, undefined (1991).
- [19] O. A. Mukhanov, Energy-efficient single flux quantum technology, *IEEE Trans. Appl. Supercond.* **21**, 760 (2011).
- [20] N. Takeuchi, T. Yamae, H. Suzuki, and N. Yoshikawa, An adiabatic superconductor comparator with 46 nA sensitivity, *IEEE Trans. Appl. Supercond.* **31**, 1 (2021).
- [21] R. McDermott and M. G. Vavilov, Accurate Qubit Control with Single Flux Quantum Pulses, *Phys. Rev. Appl.* **2**, 014007 (2014).
- [22] O. Mukhanov, A. Kirichenko, C. Howington, J. Walter, M. Hutchings, I. Vernik, D. Yohannes, K. Dodge, A. Ballard, B. L. T. Plourde, A. Opremcak, C.-H. Liu, and R. McDermott, in *2019 IEEE International Electron Devices Meeting (IEDM)* (IEEE, San Francisco, CA, USA, 2019), p. 31.2.1.
- [23] L. C. G. Govia, E. J. Pritchett, C. Xu, B. L. T. Plourde, M. G. Vavilov, F. K. Wilhelm, and R. McDermott, High-fidelity qubit measurement with a microwave-photon counter, *Phys. Rev. A* **90**, 062307 (2014).
- [24] C. Howington, A. Opremcak, R. McDermott, A. Kirichenko, O. A. Mukhanov, and B. L. T. Plourde, Interfacing superconducting qubits with cryogenic logic: Readout, *IEEE Trans. Appl. Supercond.* **29**, 1 (2019).
- [25] A. Lupaşcu, S. Saito, T. Picot, P. C. de Groot, C. J. P. M. Harmans, and J. E. Mooij, Quantum non-demolition measurement of a superconducting two-level system, *Nat. Phys.* **3**, 119 (2007).
- [26] M. Hosoya, W. Hioe, J. Casas, R. Kamikawai, Y. Harada, Y. Wada, H. Nakane, R. Suda, and E. Goto, Quantum flux parametron: A single quantum flux device for Josephson supercomputer, *IEEE Trans. Appl. Supercond.* **1**, 77 (1991).
- [27] N. Takeuchi, D. Ozawa, Y. Yamanashi, and N. Yoshikawa, An adiabatic quantum flux parametron as an ultra-low-power logic device, *Supercond. Sci. Technol.* **26**, 035010 (2013).
- [28] N. Takeuchi, Y. Yamanashi, and N. Yoshikawa, Reversible logic gate using adiabatic superconducting devices, *Sci. Rep.* **4**, 1 (2014).
- [29] N. Takeuchi, S. Nagasawa, F. China, T. Ando, M. Hidaka, Y. Yamanashi, and N. Yoshikawa, Adiabatic quantum-flux-parametron cell library designed using a 10 kA cm⁻² niobium fabrication process, *Supercond. Sci. Technol.* **30**, 035002 (2017).
- [30] S. Poletto, F. Chiarello, M. G. Castellano, J. Lisenfeld, A. Lukashenko, C. Cosmelli, G. Torrioli, P. Carelli, and A. V. Ustinov, Coherent oscillations in a superconducting tunable flux qubit manipulated without microwaves, *New J. Phys.* **11**, 013009 (2009).
- [31] M. G. Castellano, F. Chiarello, P. Carelli, C. Cosmelli, F. Mattioli, and G. Torrioli, Deep-well ultrafast manipulation of a SQUID flux qubit, *New J. Phys.* **12**, 043047 (2010).
- [32] F. Chiarello, E. Paladino, M. G. Castellano, C. Cosmelli, A. D’Arrigo, G. Torrioli, and G. Falci, Superconducting qubit manipulated by fast pulses: Experimental observation of distinct decoherence regimes, *New J. Phys.* **14**, 023031 (2012).
- [33] J. R. Johansson, P. D. Nation, and F. Nori, QuTiP 2: A Python framework for the dynamics of open quantum systems, *Comput. Phys. Commun.* **184**, 1234 (2013).
- [34] L. O. Castaños and A. Zuñiga-Segundo, The forced harmonic oscillator: Coherent states and the RWA, *Am. J. Phys.* **87**, 815 (2019).
- [35] R. McDermott, R. W. Simmonds, M. Steffen, K. B. Cooper, K. Cicak, K. D. Osborn, S. Oh, D. P. Pappas, and J. M. Martinis, Simultaneous state measurement of coupled Josephson phase qubits, *Science* **307**, 1299 (2005).
- [36] A. G. Kofman, Q. Zhang, J. M. Martinis, and A. N. Korotkov, Theoretical analysis of measurement crosstalk for coupled Josephson phase qubits, *Phys. Rev. B* **75**, 014524 (2007).
- [37] T. L. Robertson, B. L. T. Plourde, T. Hime, S. Linzen, P. A. Reichardt, F. K. Wilhelm, and J. Clarke, Superconducting quantum interference device with frequency-dependent damping: Readout of flux qubits, *Phys. Rev. B* **72**, 024513 (2005).
- [38] M. Steffen, F. Brito, D. DiVincenzo, S. Kumar, and M. Ketchen, Decoherence of floating qubits due to capacitive coupling, *New J. Phys.* **11**, 033030 (2009).
- [39] Daniel A. Lidar, Lecture notes on the theory of open quantum systems, *ArXiv:1902.00967* (2019).
- [40] Daniel Manzano, A short introduction to the Lindblad master equation, *AIP Adv.* **10**, 025106 (2020).
- [41] N. Y. Haboubi and R. D. Montgomery, *The Theory of Open Quantum Systems* (Oxford University Press, Oxford, UK, 1992), Vol. 21.
- [42] A. Isar, A. Sandulescu, and W. Scheid, Lindblad master equation for the damped harmonic oscillator with deformed dissipation, *Physica A* **322**, 233 (2003).
- [43] John Clarke and Frank K. Wilhelm, Superconducting quantum bits, *Nature* **453**, 1031 (2008).
- [44] PSCAN2 Superconducting circuit simulator, <http://www.pscan2sim.org>.
- [45] N. R. Werthamer, Nonlinear self-coupling of Josephson radiation in superconducting tunnel junctions, *Phys. Rev.* **147**, 255 (1966).
- [46] Halima Giovanna Ahmad, Luigi Di Palma, Roberta Caruso, Avradeep Pal, Giovanni Piero Pepe, Mark G. Blamire, Francesco Tafuri, and Davide Massarotti, Critical current

- suppression in spin-filter Josephson junctions, *J. Supercond. Novel Magn.* **33**, 3043 (2020).
- [47] D. R. Gulevich, L. V. Filippenko, and V. P. Koshelets, Microscopic tunneling model of Nb-AlN-NbN Josephson flux-flow oscillator, *J. Low Temp. Phys.* **194**, 312 (2019).
- [48] A. A. Odintsov, V. K. Semenov, and A. Zorin, Specific problems of numerical analysis of the Josephson junction circuit, *IEEE Trans. Magn.* **23**, 763 (1987).
- [49] A. Barone and G. Paterno, *Physics and Applications of the Josephson Effect* (John Wiley & Sons, New York, 1982), p. 25. Chapter 2.
- [50] Y. Harada, H. Nakane, N. Miyamoto, U. Kawabe, E. Goto, and T. Soma, Basic operations of the quantum flux parametron, *IEEE Trans. Magn.* **23**, 3801 (1987).
- [51] Naoki Takeuchi, Yuki Yamanashi, and Nobuyuki Yoshikawa, Energy efficiency of adiabatic superconductor logic, *Supercond. Sci. Technol.* **28**, 015003 (2014).
- [52] F. Tafuri, *Fundamentals and Frontiers of the Josephson Effect* (Springer Series in Materials Science, 2019), p.248. Chapter 7.4.
- [53] D. Yohannes, M. Renzullo, J. Vivalda, A. C. Jacobs, M. Yu, J. Walter, A. F. Kirichenko, I. V. Vernik, and O. A. Mukhanov, High Density Fabrication Process for Single Flux Quantum Circuits, *Appl. Phys. Lett.* **122**, 212601 (2023).
- [54] Oleg A. Mukhanov, Energy-efficient single flux quantum technology, *IEEE Trans. Appl. Supercond.* **21**, 760 (2011).
- [55] D. E. Kirichenko, S. Sarwana, and A. F. Kirichenko, Zero static power dissipation biasing of rsfq circuits, *IEEE Trans. Appl. Supercond.* **21**, 776 (2011).
- [56] M. H. Volkmann, A. Sahu, C. J. Fourie, and O. A. Mukhanov, Implementation of energy efficient single flux quantum digital circuits with sub-aJ/bit operation, *Supercond. Sci. Technol.* **26**, 015002 (2012).
- [57] M. Wulf, Zhou Xingxiang, J. L. Habif, P. Rott, M. F. Bocko, and M. J. Feldman, An unshunted comparator as a device for quantum measurements, *IEEE Trans. Appl. Supercond.* **13**, 974 (2003).
- [58] Tom Ohki, Alexander Savin, Juha Hassel, Leif Gronberg, Tatiana Karminskaya, and Anna Kidiyarova-Shevchenko, Balanced comparator for RSFQ qubit readout, *IEEE Trans. Appl. Supercond.* **17**, 128 (2007).
- [59] Thomas J. Walls, Timur V. Filippov, and Konstantin K. Likharev, Quantum Fluctuations in Josephson Junction Comparators, *Phys. Rev. Lett.* **89**, 217004 (2002).
- [60] Austin G. Fowler, Matteo Mariani, John M. Martinis, and Andrew N. Cleland, Surface codes: Towards practical large-scale quantum computation, *Phys. Rev. A* **86**, 032324 (2012).